P-30

Cyclotron Maser and Plasma Wave Growth in Magnetic Loops

Russell J. Hamilton [1] and Vahé Petrosian [2]

Center for Space Science and Astrophysics

Stanford University

Stanford, California

National Aeronautics and Space Administration Grant NSG-7092

National Science Foundation Grant ATM 8705084

[1] Also Department of Physics, Stanford University

[2] Also Department of Applied Physics, Stanford University

Abstract

Cyclotron maser and plasma wave growth which results from electrons accelerated in magnetic loops are studied. The evolution of the accelerated electron distribution is determined by solving the kinetic equation including Coulomb collisions and magnetic convergence. We find that for modest values of the column depth of the loop the growth rates of instabilities are significantly reduced and that the reduction is much larger for the cyclotron modes than for the plasma wave modes. The large decrease in the growth rate with column depth suggests that solar coronal densities must be much lower than commonly accepted in order for the cyclotron maser to operate. The density depletion has to be similar to that which occurs during auroral kilometric radiation events in the magnetosphere.

The resulting distributions are much more complicated than the idealized distributions used in many theoretical studies, but the fastest growing mode can still simply be determined by the ratio of electron plasma to gyrofrequency, $U = \omega_p/\Omega_e$. However, the dominant modes are different than for the idealized situations with growth of the z-mode largest for $U \lesssim 0.5$, and second harmonic x-mode (s=2) or fundamental o-mode (s=1) the dominant modes for $0.5 \lesssim U \lesssim 1$. The electron distributions typically contain more than one inverted feature which could give rise to wave growth. We show that this can result in simultaneous amplification of more than one mode with each mode driven by a different feature and can be observed, for example, by differences in the rise times of the right and left circularly polarized components of the associated spike bursts.

Subject headings: earth: aurorae - hydromagnetics - particle acceleration - radiation mechanisms - Sun: corona - Sun: radio radiation - wave motions

I. Introduction

Rapidly fluctuating, short duration (1–100 ms) spike bursts with very high brightness temperatures ($\gtrsim 10^{12}$K), high degrees of circular polarization (often up to 100%), and narrow bandwidth ($\Delta\omega/\omega \lesssim 0.01$–$0.1$) have been observed at microwave frequencies from the solar corona (Dröge 1977, Slottje 1978, Zhao and Jin 1982, Stähli and Magun 1986) and from the dwarf M star AD Leonis (Lang and Wilson 1986). Similar emissions, but of longer duration have been observed from the stellar system Algol (Lestrade *et al.*1988) and other red dwarf (dMe) flare stars (Bastian and Bookbinder 1987, Kundu and Shevgaonkar 1988). The auroral kilometric radiation (AKR) in the Earth's magnetosphere (e.g. Gurnett 1974, or more recently Calvert 1981), Jovian decameter radiation (DAM), and Saturnian (Carr, T.D., Desch, M.D., and Alexander, J.K. 1983) and Uranian (Gurnett *et al.*1986) kilometer radiation also have similar characteristics. A common feature of all these objects is that they contain energetic electrons in magnetic loop structures and the frequencies of the bursts are on the order of the electron gyrofrequency for the magnetic field strengths and electron energies expected in their magnetospheres.

The properties of the emission indicate that the radiation mechanism is not spontaneous, but is coherent emission from electrons within the magnetic structure. Wu and Lee (1979) were first to recognize that the cyclotron resonance is important for nonrelativistic or midly relativistic electrons and that the dynamics of electrons of these energies in the Earth's auroral zone can lead to an inverted momentum distribution which gives rise to amplified cyclotron emission (also known as cyclotron maser emission). This has become the accepted mechanism of AKR and has been suggested to explain solar and stellar spike bursts (Holman, Eichler, and Kundu 1980, Melrose and Dulk 1982a). Since then much theoretical work has been done to advance our basic understanding of cyclotron maser emission (Lee and Wu 1980, Hewitt, Melrose, and Rönnmark 1982, Sharma, Vlahos, and Papadopoulos 1982, Wu *et al.*1982, Freund *et al.*1983, Melrose, Hewitt, and Dulk 1984, Wu 1985). These works have established the relationship between the amplified cyclotron

emission and idealized inverted electron distributions (e.g. so called sin-N loss cone, hollow beam, and DGH distributions) which are used to make the calculations tractable. It has been shown through these studies that, in all cases, the ratio of the electron plasma frequency to gyrofrequency, $U = \omega_p/\Omega_e$, determines the fastest growing mode. The basic results are that for small $U < U_0 < 1$ the fundamental (s=1) x-mode is the fastest growing mode, for slightly larger $U \lesssim 1$, the emission is fundamental z-mode or o-mode, and as U is increased further the dominant mode changes from z-mode to second harmonic (s=2) x-mode to second harmonic o-mode. For example, for the sin-N loss cone distribution $U_0 = 0.3$ (see e.g. Melrose, Hewitt, and Dulk 1984, Fig. 1). We parenthetically add that the cyclotron maser mechanism has also been suggested to be the underlying physical process responsible for metric and decimetric continuum bursts from the sun (Winglee and Dulk 1986), localized heating of the corona (Melrose and Dulk 1982b), and particle acceleration (Sprangle and Vlahos 1983).

In general, one requires a knowledge of the momentum distribution of electrons for determination of the characteristics of the instabilities and of the associated emission properties. However, with the exception of the description of the electrons in the auroral zone by Wu *et al.*(1982) or in coronal loops by White, Melrose, and Dulk (1986, hereafter WMD86), all of the theoretical discussions have assumed some idealized electron distribution with little attention to the details of how such inverted distributions are actually realized. The standard paradigm is that electrons are accelerated (or heated) in a magnetic loop with converging field structure. Then, after reflection their distribution is inverted due to an excess of perpendicular momentum ($\partial f/\partial p_\perp > 0$) with the form of the inverted distribution given by an idealized analytic form. The inversion gives rise to coherent emission, in either the x-mode, o-mode, z-mode, or some combination of these depending on the value of U in the source. These investigations have merely shown that this simple model can account for the general aspects of the observed spike bursts.

There are, however, a few shortcomings of the theory in its simplest form. For example:

i) Typically, very high degrees (nearly 100%) of circularly polarized radiation are expected in the sense of the fastest growing mode with right (left) circularly polarized emission corresponding to the x-mode (o-mode), but for the majority of solar millisecond spike bursts the observed circular polarization is between 25 and 30% (Benz 1986).

ii) The spike bursts generally occur during the rise and maximum phase of the impulsive microwave emission (Slottje 1978, Zhao and Jin 1982, Zhao 1983) while formation of a loss cone distribution occurs after trapping and many bounce periods (see e.g. Aschwanden and Benz 1988).

iii) The growth rates (amplification factors) computed using the distribution measured *in situ* by the S3-3 satellite in the Earth's auroral zone (which shows both loss cone and hole structures) are much lower than those found from the idealized distributions and are not large enough to account for the observed levels of AKR (Omidi and Gurnett 1984). However, as pointed out by the authors in their article, the lower growth rates may be attributable to relaxation of the distribution before measurements were made or to the difficulty of measuring sharp discontinuities.

All of these indicate that the actual distributions of electrons present in physical magnetic loops are probably much more complicated than the idealized distributions assumed in the above studies. In order to evaluate the importance of departures from the idealized situations it is necessary to consider the dynamics of accelerated electrons in magnetic loops. WMD86 examined electron propagation effects in a model where electrons are impulsively heated at the apex of a converging magnetic loop, but did not include any stochastic scattering or energy loss processes e.g. Coulomb collisions. Furthermore, they compute the growth rates at times when the electrons are moving predominantly downward, while growth rates obtained after reflection are of primary interest because this is when the loss cone feature and maser action are expected to appear.

The purpose of this paper is to remove these limitations of the model by considering the transport and evolution of the electron distribution in detail. In addition to mag-

netic mirroring, other physical interactions can be important. The relevant processes to consider are determined by the energy of the electrons and the properties of the ambient plasma. For example, energy loss and pitch angle scattering due to Coulomb interactions are the dominant processes for electrons of energy 10 to 10^3 keV in flaring solar coronal loops (densities 10^9 to $10^{11}\mathrm{cm}^{-3}$ and magnetic field strengths $\sim 10^2$ to 10^3 G). These and other interactions with the ambient plasma tend to smooth out the inverted features in the electron distribution and therefore reduce the growth rates and alter emission properties of the cyclotron maser. In this article, we determine the evolution of the energetic electron distribution including Coulomb interactions as well as magnetic mirroring and then examine the subsequent effects on the growth rates of the cyclotron maser and plasma waves for different values of the field convergence and plasma density. We do not calculate the evolution of the wave spectrum and therefore do not include any nonlinear (or quasi-linear) effects on the electron distribution.

In §II, we review the wave modes of interest and the relation between these modes and the momentum distribution of electrons and also discuss the method used to compute the growth rates. In §III, we give the kinetic equation which determines the evolution of electrons in magnetic loops and describe its solution. Then, in §IV, we use this solution to compute the growth rates for cyclotron maser and plasma wave emission for a wide range of physical conditions. We discuss our results in §V.

II. Wave Properties and Growth Rate Formulae

a) Electron Cyclotron Maser

The electron cyclotron maser is associated with induced emission of the magnetoionic modes of plasma theory. The modes are the solutions to the dispersion equation for a cold plasma (collision frequency $\ll \omega_p, \Omega_e$) in a uniform magnetic field at frequencies where the motion of the ions can be neglected (see e.g. Stix 1962, p.38). The wave properties are completely determined by the two ratios $X = \omega_p^2/\omega^2$ and $Y = \Omega_e/\omega$, where ω is the wave

frequency, and the angle θ between the wave vector $\mathbf{k}$ and the direction of the magnetic field. There are two solutions to the dispersion equation at each frequency and we adopt the conventions of Melrose (1980b, p. 258) to describe these modes and their growth rates. The wave properties, namely the index of refraction $n_\sigma = k_\sigma c/\omega$, the longitudinal part of the polarization K_σ, and the axial ratio of the polarization ellipse T_σ, of mode σ (-1 for x-mode, $+1$ for o-mode) are

$$n_\sigma^2 = 1 - \frac{XT_\sigma}{T_\sigma - Y\cos\theta} , \tag{1}$$

$$K_\sigma = \frac{XY\sin\theta}{1-X}\frac{T_\sigma}{T_\sigma - Y\cos\theta} , \tag{2}$$

$$T_\sigma = -\sigma(x^2+1)^{1/2} - x , \tag{3}$$

$$x = \frac{Y\sin^2\theta}{2(1-X)\cos\theta} . \tag{4}$$

The resonant ($n_\sigma^2 = \infty$) and cut-off ($n_\sigma^2 = 0$) frequencies determine the frequency range where these modes propagate. The waves propagate above their cut-off frequency which is equal to the plasma frequency, ω_p, for the o-mode, and a frequency

$$\omega_x = \frac{\Omega_e}{2}[1 + (1+4U^2)^{1/2}] , \tag{5}$$

for the x-mode. For frequencies below the cut-off, but larger than the resonant frequency the waves decay. The resonant frequencies are

$$\omega_\pm^2(\theta) = \frac{\Omega_e^2}{2}\left(1 + U^2 \pm [(1+U^2)^2 - 4U^2\cos^2\theta]^{1/2}\right) , \tag{6}$$

where $+$ is for the x-mode and $-$ for the o-mode. Note that the usual sign convention, which we use here, is opposite to the usual sign convention used for σ above. Below the resonant frequencies the modes change character. The x-mode becomes the z-mode which propagates in the frequency range $\omega_x - \Omega_e < \omega < \omega_+$. The z-mode can not escape a physical plasma because it will eventually be absorbed in a lower density region where its frequency equals the resonant frequency ω_+. Below ω_-, the o-mode becomes the whistler which will not be of interest here.

The electron cyclotron maser action is possible when the electron momentum distribution is such that amplification (negative damping) of these modes occurs. Near resonances one must include the effects of finite temperature of the plasma. This changes the dispersion relation and wave properties given here for the cold plasma modes. Below, we discuss waves near the resonances further and their relevance to the maser problem.

i) General Growth Rate Equations

The growth rate $\Gamma^\sigma(\mathbf{k})$ of a particular wave (specified by mode, frequency, and angle) is given by (see e.g. Melrose 1980b, p. 275)

$$\Gamma^\sigma(\mathbf{k}) = \sum_{s=-\infty}^{\infty} \int A_s^\sigma(\mathbf{k},\mathbf{p})\delta(\omega - s\Omega_e/\gamma - k_\parallel \beta_\parallel c) \left(\frac{s\Omega_e}{\gamma\beta_\perp c}\frac{\partial}{\partial p_\perp} + k_\parallel \frac{\partial}{\partial p_\parallel}\right) f(p_\parallel, p_\perp) 2\pi p_\perp dp_\perp dp_\parallel, \tag{7}$$

where the transition rate A_s^σ is

$$A_s^\sigma(\mathbf{k},\mathbf{p}) = \frac{(2\pi e c\beta_\perp)^2}{\omega n_\sigma \frac{\partial(\omega n_\sigma)}{\partial\omega}(1+T_\sigma^2)} \left| \frac{K_\sigma \sin\theta + (\cos - n_\sigma\beta_\parallel)T_\sigma}{n_\sigma \beta_\perp \sin\theta} J_s(z) + J_s'(z) \right|^2 , \tag{8}$$

J_s is the bessel function of order s, its argument $z = \gamma n_\sigma \beta_\parallel \sin\theta / Y$, and

$$n_\sigma \frac{\partial(\omega n_\sigma)}{\partial\omega} = 1 + \frac{XYT_\sigma \cos\theta}{2(T_\sigma - Y\cos\theta)^2}\left(1 + \frac{(1+X)(1-T_\sigma^2)}{(1-X)(1+T_\sigma^2)}\right) . \tag{9}$$

Including only the $s = n$ term in equation (7) gives the growth rate of the n^{th} harmonic of a particular mode σ (e.g. $\sigma = -1$, $s = 1$, yields the growth rate of the fundamental x-mode). The resonance condition given by the δ function in equation (7) reduces the integral to a one-dimensional integral along an ellipse in velocity space (hyperbola in momentum space) which is called the resonance ellipse. This condition severely limits the electron energies which contribute to the growth of a particular wave. Furthermore, the cyclotron maser is driven by nonrelativistic electrons therefore the argument of the bessel function is small $z \ll 1$ and $J_s(z) \sim z^s$ so that the growth rates are largest for the first few harmonics. Therefore, the growth rate of a wave is dominated by a particular term (harmonic) in the sum so that it is useful to discuss the growth at different harmonics separately.

ii) Equations for Nonthermal Electron Distributions

Given the electron distribution f, calculation of the growth rates for the various modes is straightforward. As described in the next section, we will use the kinetic equation to obtain a solution for the electron distribution f as function of E and μ. The transformation of variables necessary to apply the growth rate formula of equation (7) is obtained from $f(E,\mu) = \gamma^2\beta m^3c^3 f(p_\parallel, p_\perp)$, which gives

$$\Gamma_s^\sigma(\mathbf{k}) = \int dE \frac{(A_s^\sigma/mc^2)}{n_\sigma|\cos\theta|}\left[\gamma^2\frac{\partial}{\partial E} + \frac{\gamma}{\beta^2}(n_\sigma\beta\cos\theta - \mu)\frac{\partial}{\partial\mu}\right]\left(\frac{f(E,\mu)}{\gamma^2\beta}\right)\Bigg|_{\mu=\mu_R}, \qquad (10)$$

where $\mu_R = (1 - sY/\gamma)/\beta n_\sigma\cos\theta$. In general, f is the sum of the distribution of thermal background plasma and the nonthermal electrons whose distribution is obtained from equation (20) below. The background thermal plasma (with total density n_0) gives a negative contribution to the growth rate which we will consider separately, so that, unless otherwise specified, in what follows f stands for the normalized ($\int f dE d\mu$=1) nonthermal component of the distribution with total density n_a. After further simplification, we find that the ratio of the growth rate to the gyrofrequency is

$$\frac{\Gamma_s^\sigma(\mathbf{k})}{\Omega_e} = \frac{n_a}{n_0}\frac{\pi U^2 Y}{B_\sigma(\mathbf{k})}\int dE\Bigg|[K_\sigma\sin\theta + (\cos\theta - n_\sigma\beta\mu_R)T_\sigma]J_s(z) + \beta_\perp n_\sigma\sin\theta J_s'(z)\Bigg|^2 \qquad (11)$$
$$\left[\gamma^2\frac{\partial}{\partial E} + \frac{\gamma}{\beta^2}(n_\sigma\beta\cos\theta - \mu)\frac{\partial}{\partial\mu}\right]\left(\frac{f(E,\mu)}{\gamma^2\beta}\right)\Bigg|_{\mu=\mu_R},$$

$$B_\sigma(\mathbf{k}) = n_\sigma^3\sin^2\theta|\cos\theta|\left((1+T_\sigma^2) + \frac{XYT_\sigma\cos\theta(1-XT_\sigma^2)}{(T_\sigma - Y\cos\theta)^2(1-X)}\right). \qquad (12)$$

The calculation of the growth rate for any wave is straightforward using these equations if the distribution f is known. However, given f the determination the wave having the largest growth rate is not. In §IV below, we discuss an efficient method for this determination.

We have tested this method of growth rate calculation and our expression for the growth rate given in equations (11) and (12) by computing the maximum growth rates for the sin-N loss cone distribution

$$\tilde{f}(\beta,\alpha) = \frac{(2\pi)^{-3/2}}{\beta_T^3}\exp(-\beta^2/2\beta_T^2)\begin{cases}\sin^N(\pi\alpha/2\alpha_c), & \alpha\le\alpha_c\\ 1, & \alpha>\alpha_c\end{cases} \qquad (13)$$

where $f(E,\mu) = \gamma^3 \beta \tilde{f}(\beta,\alpha)$, $N = 6$, $\alpha_c = 30°$, and $\beta_T = \sqrt{kT/mc^2}$ (with $T = 10^8$K), and comparing our results to those of Melrose, Hewitt, and Dulk (1984, Fig. 1) and Aschwanden and Benz (1988, Fig. 5). We confirm these calculations. However, we note that our convention (see also Sharma, Vlahos, and Papadopoulos 1982) is to combine the factor of the ratio of the densities with the growth rate, while these previous works fix the density ratio (10^{-2}) for a particular value of U (0.1). There is then a difference of a density factor in the expressions for the growth rates, but the relative growth rates of the given modes are identical for any value of U.

b) Plasma Waves

In addition to maser emission, the distribution of accelerated electrons is expected to generate longitudinal waves (or plasma waves), especially when the electrons are predominantly down going and therefore beam-like (see e.g. Hamilton and Petrosian 1987). In a magnetized plasma, these waves occur near a resonance of the magnetoionic modes with the value of U determining the resonance $\omega_+(\theta)$ or $\omega_-(\theta)$. Near these frequencies, the wavelength becomes smaller than the Debye length and thermal corrections to the wave properties are then necessary (Melrose 1980, p. 265). For $U < 1$, the resonance at $\omega = \omega_-(\theta)$ yields a longitudinal mode which is usually called the slow plasma wave. For $U > 1$, the longitudinal mode occurs at the resonance $\omega = \omega_+(\theta)$ and is called the generalized Langmuir wave.

The growth rate of generalized Langmuir waves ($U > 1$) was examined by McClements (1987) to determine the stability of the steady state solutions of Leach and Petrosian (1981) and in WMD86 the growth rate of the slow plasma wave ($U < 1$) is evaluated for down going electrons. One finds in both of these papers that the maximum growth rate occurs at $\theta = 0$. Therefore, we evaluate the growth rate of plasma waves when the wave vector is along the magnetic field ($\theta = 0$). This simplifies the analysis because, regardless of the

value of U, the frequency of these waves is given by

$$\omega_l^2 = \omega_p^2 + 3k^2 v_e^2 \ , \tag{14}$$

where $v_e^2 = kT_e/m_e$ is the thermal velocity of electrons in the ambient plasma of temperature T_e. For this angle of propagation only the $s = 0$ term in the sum of equation (7) is nonzero and the growth rate can be written

$$\frac{\Gamma_l}{\omega_p} = \frac{n_a}{n_0}\frac{\pi\omega_p}{n_l^3\omega_l}\int dE\left[\gamma^2\frac{\partial}{\partial E} + \frac{\gamma}{\beta^2}\frac{(1-\mu^2)}{\mu}\frac{\partial}{\partial\mu}\right]\left(\frac{f(E,\mu)}{\gamma^2\beta}\right)\Bigg|_{\mu=1/n_l\beta} \ . \tag{15}$$

Thermal damping must also be considered for the plasma modes. This provides a negative contribution of

$$\frac{\Gamma_T}{\omega_p} = -\sqrt{\frac{\pi}{2}}\frac{\omega_p}{\omega_l}\frac{1}{n_l^3\beta_T^3}\exp(-1/2n_l^2\beta_T^2) \ , \tag{16}$$

so that the total growth rate is given by the sum of equations (15) and (16).

III. Electron Dynamics and Distribution

As discussed above, in most models of maser emission it is argued that the electron distribution is given by an idealized functional form such as the sin-N loss cone (see eq. [13]) and the emission properties are studied using growth rates computed using this idealized distribution. In this section, we present a more realistic model in which a specified electron distribution is injected in a magnetic loop. The electron distribution resulting from subsequent evolution and transport of the electrons in the magnetic loop which determines the growth rate of the modes is found by solving the electron kinetic equation using the Fokker-Planck formalism. This allows us to determine how the strength and degree of convergence of the magnetic field and the plasma density effect the maser action.

a) Kinetic Equation

The propagation and evolution of accelerated electrons in magnetic loops is determined by the kinetic equation. For electrons of energy 10 keV to 1 MeV in an ambient plasma with density 10^9 to $10^{14}\mathrm{cm}^{-3}$ and magnetic field strength 10^2 to 10^3 G (conditions

believed to occur in the coronae of the sun and flare stars with $\Omega_e \sim 0.3$ to 3 GHz) the dominant processes are magnetic mirroring, Coulomb collisions, and wave-particle interactions. Observations allow us to estimate with some degree of confidence the expected effects of the first two processes, but we lack direct knowledge of the amount of plasma waves that are present in the flare plasma. The minimal level of plasma waves is that produced by the instabilities which we are about to evaluate. As mentioned above, inclusion of the back reaction of the waves generated by electrons on their propagation is a nonlinear problem which increases the complexity of the situation beyond the scope of this paper. The steady state problem for $U \gg 1$ (only Langmuir waves) including the effects of collisions and the nonlinear effects of waves was treated in our earlier paper (Hamilton and Petrosian 1987). In this paper, we ignore the uncertain effects of the plasma waves so that the evolution of the electron distribution in a cold plasma ($kT \ll$ typical electron energy) is determined by (see e.g. Hamilton, Lu, and Petrosian 1990)

$$\frac{\partial f}{\partial t} = -\beta c\mu \frac{\partial f}{\partial s} + \beta c \frac{d\ln B}{ds}\frac{\partial}{\partial \mu}\left(\frac{(1-\mu^2)}{2} f\right) + \frac{c}{\lambda_0}\frac{\partial}{\partial E}\left(\frac{f}{\beta}\right) + \frac{c}{\lambda_0 \beta^3 \gamma^2}\frac{\partial}{\partial \mu}\left[(1-\mu^2)\frac{\partial f}{\partial \mu}\right] + S \ , \tag{17}$$

where $\lambda_0 = (10^{24}\mathrm{cm})/n_0(s)\ln\Lambda$, $n_0(s)$ is the background plasma density, $\ln\Lambda(\approx 20)$ is the Coulomb logarithm, and $S(E,\mu,s,t)$ is the source. Here we have assumed that the electron gyroradius is much smaller than other relevant length scales (i.e. λ_0 or $(d\ln n_0/ds)^{-1}$) so that the electron distribution function $f(E,\mu,s,t)$ can be described by four variables, the particle kinetic energy E (in units of mc^2), pitch angle cosine μ, position along the magnetic field s, and the time t.

b) The Source Term

The existence of nonthermal electrons with energies of 10 to 100 keV in solar coronal loops is well established from studies of impulsive hard X-ray bursts (see e.g. Kane *et al.*1980). The electrons are characterized by a power-law energy spectrum $f(E) \propto E^{-\delta}$ with $2.5 \lesssim \delta \lesssim 7.5$, but the angular distribution is not very well known (see e.g. McTiernan

and Petrosian 1990). Electrons of these energies (10 to 100 keV) accelerated on open field lines (or on closed field lines of very large radii) are also believed to be the source of type III radio bursts (Goldman and Smith 1986). It is therefore natural to assume that under certain circumstances such accelerated electrons when reflected before reaching the transition region can be a source of free energy to drive the cyclotron maser. This assumption is supported by the association of the impulsive hard X-ray and spike emissions (see Benz and Kane 1986). Similar energetic particle spectra are expected to be present in other flare stars.

Hence, we will assume a source function

$$S(E,\mu,s,t) = \frac{n_a}{2(\delta-1)E_0}(E_0/E)^\delta \exp(-s^2/L_a^2)\delta(t) \ . \tag{18}$$

This corresponds to the impulsive acceleration of electrons with an isotropic pitch angle distribution and power-law index δ within an acceleration region of characteristic size L_a. The distribution is normalized such that the density of nonthermal electrons of energy greater than E_0 at $s = 0$ is n_a.

c) The Ambient Plasma

We assume, as is generally done, that the above distributions of electrons are injected into a symmetric coronal loop of half length L_c with apex at $s = 0$. As is evident from equation (17), in addition to the source term S, we also need to specify the plasma parameters λ_0 and $d\ln B/ds$ and their variation along the loop which are obtained from the variations of plasma density $n_0(s)$ and field strength $B(s)$, respectively. For the purpose of solving equation (17) we only need the ratio $B(s)/B_0$ where B_0 is the field strength at $s = 0$ and not the absolute magnitude of the magnetic field. Following WMD86, we adopt the simple model

$$B(s)/B_0 = 1 + s^2/L_B^2 \tag{19}$$

which corresponds to the variation of magnetic field strength in the far field of a dipole. We further assume that the density in the corona is constant and increases rapidly below

the transition region with a scale height much shorter than L_B or L_c so that particles which reach there are quickly thermalized and do not contribute to the maser emission.

The extent of the loss cone distribution is determined by the ratio L_B/L_c or by what we call the mirror ratio $r_m = 1 + L_c^2/L_B^2$ which is defined such that, in the absence of collisions, electrons injected (at $s = 0$) with pitch angles greater than $\alpha_c = \arcsin(1/\sqrt{r_m})$ are reflected above the transition region. On the other hand, the degree to which the collisions smooth out loss cones is determined by the column depth to the transition region $N_{tr} = n_0 L_c$.

d) Solution of the Kinetic Equation

We have solved the kinetic equation (17) using the numerical code described in Hamilton, Lu, and Petrosian (1990) for the impulsive source given by equation (18) with $L_a = 0.1 L_c$ and $\delta = 5$. For the ambient plasma, we use $r_m = 1$, 2, 5, and 10 and column depths to the transition region $N_{tr} = 0$, 1.91×10^{17}, 4.74×10^{18}, 1.88×10^{19}, 7.37×10^{19}, and $4.36 \times 10^{20}\mathrm{cm}^{-2}$. Since the column depth an electron of energy E traverses before stopping is

$$N(E) = n_0 \lambda_0 E^2/(E+1) \ . \tag{20}$$

the above column depths (N_{tr}) correspond to the stopping depths for electrons of initial energies $E = 0$, 1, 5, 10, 20, and 50 keV, respectively. Strictly speaking, no plasma modes can be expected for $N_{tr} = 0$ or for zero density plasma. This case represents the idealized situation for which collisions can be neglected and provides a useful comparison for the finite density situations where collisions with the ambient plasma become increasingly important (cf. White, Melrose, and Dulk 1983). This case will also be useful for comparison with the results of WMD86 who ignored collisions.

It should be noted that the results presented below are more general because of the simple scaling properties of the kinetic equation (17). The dynamics are completely determined by the column depth $N_{tr} = n_0 L_c$ and the mirror ratio r_m. Rescaling the variables

in the kinetic equation according to the transformations $L' = \eta L$ for all the lengths in the problem, $n' = n/\eta$ for the densities, and $t' = \eta t$ for the time, leaves the equation unchanged. Therefore, if the kinetic equation is solved for a given half loop length L_c, density n_0, and mirror ratio r_m, the solution for this mirror ratio and column depth $N_{tr} = n_0 L_c$ is obtained for any half loop length $L'_c = \eta L_c$ and density $n'_0 = n_0/\eta$ by transforming the time $t' = \eta t$, position $s' = \eta s$, and $L'_s = \eta L_s$.

Some of the results from these calculations are shown in Figures 1 and 2 where we present contour plots in velocity space ($\beta_\parallel$, $\beta_\perp$) of the distribution function at four times (described below) and at two locations $s = 0$ and $s = L_c/2$, respectively. The mirror ratio $r_m = 5$ corresponds to $L_c/L_B = 2$ or critical pitch angle $\alpha_c = 26°$ ($\mu_c^2 = 0.8$). On each figure, the left, middle, and right panels are for column depths corresponding to stopping depths for electron energies $E = 0$, 10, and 20 keV, respectively. In the absence of collisions, electrons of initial energy E_i (or velocity β_i) and pitch angle cosine μ_i will be reflected after a time $T_B = \pi L_B/2\beta_i c\sqrt{1-\mu_i^2}$. Since we consider electrons of energy $E > E_0$ (see eq. [18]) and because only electrons with $\mu_i < \mu_c$ (or $\alpha_i > \alpha_c$) are reflected, the maximum value of interest for T_B is $T_B^{max} = \pi L_B\sqrt{r_m}/2\beta_0 c$. We use a minimum electron energy $E_0 = 10$ keV, and display from top to bottom on each figure the distribution at times $t_1 = \frac{1}{6}T_B^{max}$, $t_2 = \frac{1}{2}T_B^{max}$, $t_3 = T_B^{max}$, and $t_4 = \frac{3}{2}T_B^{max}$, respectively.

Vertical and horizontal cuts on this figure show where $\partial f/\partial|\beta_\parallel| > 0$ and $\partial f/\partial\beta_\perp > 0$ which are the features of the electron distribution that give rise to amplified emission. For example, in Figure 1 for the model $E = 0$ along the line $\beta_\parallel = 0.3$ at time t_2 there is one region and at t_3 there are three regions where $\partial f/\partial\beta_\perp > 0$. Regions of $\partial f/\partial\beta_\perp > 0$ are also seen in Figure 2 at these times. Positive gradients in parallel velocity ($\partial f/\partial|\beta_\parallel| > 0$) are most clearly seen in Figure 2 at t_1, for all values of the column depth.

We have shown contour plots in velocity space even though we calculate the distribution $f(E,\mu)$ in energy and pitch angle cosine space and the growth rate formulae are given in terms of momentum space variables (see eq. [7]). We do this because the phase space

defined by $(\beta_{\|}, \beta_{\perp})$, unlike the other variable choices, is finite and because it is common practice to display these contours in velocity space. Notice that for the energies involved there will be very little difference between the shapes of these contours and those made in momentum space so that features found in the velocity distribution here are also present in the momentum distribution. No contours are shown for $\beta < 0.2$ because $E_0 = 10$ keV is the lowest energy considered in our calculations.

Comparison of the two figures shows that the distributions at the top of the loop are markedly different than distributions midway down the loop. This would indicate that the emission properties such as polarization, frequency, angle, and brightness temperature will vary along the loop. Comparison of the contours for different column depths shows that the effect of the collisions is to smooth out the sharp features of the distribution which are the source of instabilities so that even for modest column depths ($N_{tr} \gtrsim 7.37 \times 10^{19}\mathrm{cm}^{-2}$), the unstable features of the distribution are only seen on the lowest contours and at early times.

Note that these more realistic distributions are far from the idealized assumed distributions mentioned earlier. However, parts of these distributions resemble parts of the idealized distributions. For example, the distributions in Figure 1 at t_2 have loss cone features which are qualitatively similar to the sin-N distribution, and the distribution at t_3 for $N_{tr} = 0$ in Figure 2 shows isolated contours centered at ($\beta_{\|} \sim 0.1$, $\beta_{\perp} \sim 0.3$) which resemble the so called hollow beam distribution.

IV. Growth Rates and Analysis

As mentioned above, when determining the dynamical evolution of the distribution we need to specify the rate of convergence (or divergence) of the magnetic field, $d\ln B/ds$, but not its magnitude. However, as stated in §II, the most important parameter in determining the growth rates is the ratio of the plasma to gyrofrequency $U = (n/10^{10}\mathrm{cm}^{-3})^{1/2}(320\mathrm{G}/B)$. Therefore, to completely specify a model, in addition to the mirror ratio and the column depth, we must specify the value of U at the top of

the loop. We should also consider the effects of finite temperature even though these are unimportant for determining the particle distribution as long as $kT \ll E_0$. The primary effect here is thermal damping of the waves by the ambient plasma. However, for magnetoionic waves, damping is unimportant provided that the above inequality is valid so that particle velocities far exceed the thermal velocity v_e.

a) Cyclotron Maser

We need to compute the growth rates of x-mode, o-mode, and z-mode waves for a particular distribution f. In order to sample the frequency space (ω, θ) efficiently, we use the method outlined in Aschwanden (1989). For a given mode σ and (ω, θ) pair, the resonance condition represented by the δ-function in equation (7)

$$\omega - s\Omega_e/\gamma - k_\parallel \beta_\parallel c = 0 \tag{21}$$

defines an ellipse in velocity space $(\beta_\parallel, \beta_\perp)$,

$$\frac{(\beta_\parallel - \beta_0)^2}{V^2(1-e^2)} + \frac{\beta_\perp^2}{V^2} = 1 \ , \tag{22}$$

with the center $(\beta_0, 0)$, semi-major axis V, and eccentricity e given by

$$\begin{aligned} \beta_0 &= \frac{e^2}{n_\sigma \cos\theta} \ , \\ V &= [1 - (e/n_\sigma \cos\theta)^2]^{1/2} \ , \\ e &= [1 + (sY/n_\sigma \cos\theta)^2]^{-1/2} \ . \end{aligned} \tag{23}$$

Conversely, each point in velocity space $(\beta_\parallel, \beta_\perp)$ can be identified with the top of a resonance ellipse with $\beta_0 = \beta_\parallel$, $V = \beta_\perp$, and frequency $\omega = s\Omega_e\gamma(1-\beta_\perp^2)$. The last relation can be obtained from equation (21) using the expression $k_\parallel = k\cos\theta = n_\sigma\omega\cos\theta/c$ and the fact that at the top of the resonance ellipse $e^2 = \beta_\parallel n_\sigma \cos\theta$ and $1 - e^2 = \gamma^{-2}/(1-\beta_\perp^2)$. The frequency space grid is set-up by first finding the frequency range defined by the velocity space grid and then subdividing this range. The range of angles for each frequency is determined by the requirement that the resonant condition be satisfied (eq. [21]).

Using the formulae of §II, results of §III, and this method of calculation, we evaluate the growth rates of the x-mode ($s = 1, 2$), o-mode ($s = 1, 2$), and z-mode (s=1) for three values U_{top} = 0.1, 0.5, and 1.0. The results of our calculations are shown in Tables 1 (top of the loop) and 2 (at $s = L_c/2$) at times $t_2 = T_B^{max}$ and $t_4 = \frac{3}{2}T_B^{max}$ for three values of the mirror ratio r_m. Note that the growth rates are functions of frequency and angle and that we list the maximum values of the growth rates of each mode here. The mode having the largest growth rate for a particular time and model is bold faced. We draw the following conclusions from the results listed in these tables.

1. As the column depth of the plasma in the loop increases the growth rates decrease. This is a general trend which is independent of the values of r_m or U. Even for a modest column depth of $1.88 \times 10^{19} \mathrm{cm}^{-2}$ the growth rates are reduced by 2 to 4 orders of magnitude.

2. The mode with the largest growth rate does not remain the same throughout the entire loop because for converging magnetic field geometries the ratio U and the electron distribution vary along the loop.

3. Although the distributions are complicated and vary along the loop, there are some general trends in the results. These trends are in general different than those obtained from assumed distributions or idealized situations. The fastest growing modes are z-mode for $U \lesssim 0.5$, and second harmonic x-mode or fundamental o-mode for $0.5 \lesssim U \lesssim 1$. Fundamental x-mode growth is not important, even for $U < 0.3$. The fastest growing mode also depends on the value of the mirror ratio r_m. For example, for $U_{top} = 0.5$, the mode having the largest growth rate at the top of the loop is the second harmonic x-mode when $r_m = 2$ but changes to the fundamental o-mode for $r_m \geq 5$.

4. An important consequence of the complexity of the distribution is the presence of more than one inverted feature which occurs even at larger column depths but with reduced gradients. This leads to the possibility that each of these inverted features might drive a different instability. Since relaxation of one part of the distribution does not directly affect the other inverted features, the distribution can support growth in more than one

mode simultaneously. To illustrate this, we show in Figure 3 a contour plot of the electron distribution for the model with $N_{tr} = 1.88 \times 10^{19}\mathrm{cm}^{-2}$ and $r_m = 5$ at $s = L_c/2$ for time $t_4 = \frac{3}{2}T_B^{max}$. Overlying the contours are the resonance ellipses for the o-mode (s=1), x-mode (s=2), and z-mode (s=1) corresponding to the frequencies and angles for these modes that produced the largest growth rates given in Table 2. From the table we see that $\Gamma_1^o > \Gamma_1^z > \Gamma_2^x$, but as evident from Figure 3, these modes are driven by different features of the inverted electron distribution. Therefore, even though $\Gamma_1^o \sim 5\Gamma_2^x$, saturation of the o-mode (if it occurs) will not inhibit amplification of the x-mode. This is an important result since this provides a mechanism to explain saturated maser emission which is not very highly ($\sim$100%) circularly polarized. If the burst is resolved, a direct observational consequence is that the right and left circular polarizations will show different rise times due to the differences in the growth rates. It is clear that a more detailed analysis including the dynamics of the wave growth is required in order to quantitatively determine the time profile of the resulting spike bursts, but the qualitative behavior should agree with this description.

b) Plasma Waves

Because damping by thermal electrons is important, the growth rate does not simply scale with the ratio of the density of nonthermal to thermal electrons. The dispersion relation as well as the thermal damping rate are sensitive to the temperature of the ambient plasma. We compute the growth rate of plasma waves for $n_a/n_0 = 10^{-2}$ and 10^{-4} for $T = 10^6$ and 10^7K. In Table 3, we give the maximum growth rates of waves with wave vectors along the loop for times $t_1 = \frac{1}{6}T_B^{max}$ and $t_2 = \frac{1}{2}T_B^{max}$. As expected, increasing the column depth, increasing the temperature of the thermal plasma, or decreasing the ratio n_a/n_0 reduces the growth rate. Notice that increasing the column depth does not reduce the production of plasma waves by as large a factor as was seen for the magnetoionic modes. Also note that the growth rates are largest at early times when the electrons are down going and the distribution has beam-like nonthermal features.

Relaxation of the distribution due to the generation of plasma waves results in the reduction of the column depth traversed by the forward moving electrons (see e.g. Hamilton and Petrosian 1987), but is not expected to influence the maser action since these processes involve different electrons (cf. WMD86). However, we compute these growth rates to emphasize the fact that whenever maser action occurs in this type of a physical system it is accompanied by the production of plasma waves. Furthermore, the plasma waves are generated at earlier times because they are driven by beam features which appear in the distribution before reflection of electrons occurs. However, plasma waves could produce density fluctuations which would modulate the maser emission.

V. Discussion

We have examined the cyclotron and plasma wave growth induced by electrons accelerated in magnetic loops. We considered an initial accelerated electron distribution which is consistent with nonthermal electron distributions that produce the impulsive hard X-ray spectrum found in solar flares and is expected to be present in stellar flares as well. The evolution of the electron distribution was determined by solving the kinetic equation including magnetic convergence and Coulomb collisions with the ambient plasma. In general, the fastest growing mode is determined by the value of U, as for the idealized distributions, with z-mode dominant for $U \lesssim 0.5$, and second harmonic x-mode or fundamental o-mode for $0.5 \lesssim U \lesssim 1$. Growth of the fundamental x-mode is not significant which is in contrast to the idealized situation. The resulting distributions have a complex structure and typically have more than one inverted nonthermal feature. We showed that these features can drive different modes simultaneously and that this provides a mechanism to explain partially polarized emission. We note that it might also be possible for multiple features to give rise to simultaneous amplification of different harmonics of the same polarization (e.g. x-mode at s=1 and s=2). Plasma wave growth is also shown to occur so that if cyclotron maser emission produces the spike bursts the density fluctuations which result from the plasma waves causes variations in U which could then modulate the emission.

When collisions are included maser action still occurs, but the growth rates are reduced significantly. The growth of plasma waves is also reduced, but by a much smaller amount. Under modest conditions of column depth $N_{tr} = 1.88 \times 10^{19}\mathrm{cm}^{-2}$ the growth rates are typically reduced by 2 to 4 orders of magnitude for the magnetoionic modes and less than a factor of ten for the plasma waves. For nominal physical conditions ($L_c \sim 10^9$–10^{10}cm and $n_0 \sim 10^9$–$10^{11}\mathrm{cm}^{-3}$) in flaring solar coronal loops the column depth is this large or larger. Therefore, maser emission in such loops is expected to be severly limited. This is also true in larger ($L_c \gtrsim 10^{10}$cm) low density ($n_0 \lesssim 10^9\mathrm{cm}^{-3}$) loops which extend into the upper corona because our results depend primarily on the column depth and to a lesser extent on the the ratio of magnetic field scale height to loop length. Under these conditions, this indicates that the spikey, rapidly varying bursts might be due to plasma emission as suggested by Kuijpers, van der Post, and Slottje (1981) and not cyclotron maser emission. However, the spike bursts should then be similar to type III bursts, but the characteristic signatures of the spike and type III bursts are very different (see Benz 1986 Fig. 2). In addition, density depletions are observed to occur simultaneously with the AKR (Benson, Calvert, and Klumpar 1980). This may indicate that similar processes are occurring in planetary, solar, and stellar magnetospheres. Our results suggest that in a solar flare region, where there exists a large range of magnetic field strengths, temperatures, and densities, maser action is possible only in the regions of lower density (and presumably higher magnetic field or temperature for pressure balance) and should occur primarily at the flare onset before chromospheric evaporation increases the density suppressing the maser action. This behavior explains why the spike bursts are usually seen only during the rise and maximum phases of the microwave emission during solar flares.

Acknowledgments

We acknowledge support of this work by National Aeronautics and Space Administration grant NSG-7092 and National Science Foundation grant ATM 8705084.

Table 1

$\log\left(\frac{\Gamma_{max}}{\Omega_e}\frac{n_0}{n_a}\right)$ at the top of the loop

t:				t_2									t_4					
r_m:	2			5			10			2			5			10		
N_c:	0	10	20	0	10	20	0	10	20	0	10	20	0	10	20	0	10	20
$U_{top} = 0.1$																		
$X1$:	-6.83	-5.69	-7.87	-4.34	-5.10	-6.02	-3.05	-4.07	-5.53	-2.68	-6.73	-7.83	-2.35	-5.22	-7.22	-2.65	-5.07	-6.84
$X2$:	-4.19	-5.93	-7.19	-3.59	-5.31	-6.75	-2.41	-4.95	-5.88	-2.57	-6.34	-7.88	-1.93	-6.01	-8.15	-2.46	-6.54	-8.07
$O1$:	-5.07	-5.98	-6.81	-3.85	-4.90	-5.89	-2.36	-4.23	-5.40	-2.20	-5.98	-7.40	-2.26	-5.44	-7.09	**-1.95**	-5.28	-6.74
$O2$:	-6.14	-7.10	-7.94	-5.22	-6.30	-7.59	-4.12	-6.15	-6.77	-4.08	-7.39	-8.62	-3.96	-7.13	-8.84	-3.97	-7.51	-8.51
$Z1$:	**-3.51**	**-5.02**	**-6.12**	**-2.50**	**-4.12**	**-5.13**	**-1.17**	**-3.46**	**-4.83**	**-0.92**	**-5.20**	**-6.79**	**-0.92**	**-4.56**	**-6.32**	-2.00	**-4.63**	**-6.01**
$U_{top} = 0.5$																		
$X1$:	*	*	-9.70	-6.71	-6.68	-6.64	-6.30	-6.35	-6.53	*	*	*	-7.23	-7.23	-7.32	-6.61	-6.70	-6.95
$X2$:	**-2.81**	**-4.11**	**-5.45**	**-1.88**	-3.74	-5.02	-1.09	-3.60	-4.66	**-0.48**	-4.86	**-5.96**	**-0.64**	-4.57	-6.19	**-0.56**	-5.23	-6.01
$O1$:	-3.79	-4.61	-5.53	-1.99	**-3.69**	**-4.66**	**-1.03**	**-3.05**	**-4.14**	-0.55	**-4.74**	-6.08	-0.96	-4.07	**-5.51**	-0.68	**-4.02**	**-5.43**
$O2$:	-4.80	-5.68	-6.69	-3.79	-5.10	-6.16	-2.88	-4.78	-5.56	-3.17	-5.98	-7.31	-2.57	-5.84	-7.45	-2.32	-6.49	-7.23
$Z1$:	-3.74	-4.67	-5.94	-2.01	-3.83	-4.78	-1.42	-3.42	-4.56	-1.76	-4.89	-6.54	-1.11	**-4.00**	-5.98	-0.98	-4.14	-5.60
$U_{top} = 1.0$																		
$X1$:	*	*	*	*	*	*	*	*	*	*	*	*	*	*	*	*	*	*
$X2$:	**-1.65**	**-4.60**	**-5.84**	**-1.40**	**-2.93**	**-4.68**	**-0.62**	-2.87	-4.46	**-0.44**	**-4.01**	-6.40	**-0.24**	**-4.22**	-6.05	**-0.31**	**-4.29**	-5.94
$O1$:	-7.46	-5.68	-7.36	**-4.27**	**-4.73**	-5.46	-3.14	-3.82	-5.03	-3.04	-6.36	-7.29	-2.46	-4.88	-6.60	-2.58	-4.79	-6.19
$O2$:	-4.39	-5.19	-6.40	**-2.93**	**-4.70**	**-5.80**	-2.32	-4.41	-5.28	-1.95	-5.66	-6.67	-2.19	-5.38	-6.61	-2.24	-5.80	-7.10
$Z1$:	-4.91	-6.10	-6.46	-2.00	-3.72	-5.18	-1.71	**-2.64**	**-4.42**	-0.69	-4.79	**-6.37**	-0.45	-4.98	**-5.56**	-0.84	-4.34	**-5.22**

Values of the growth rate smaller than 10^{-10} are represented by an asterick.

Table 2

$$\log\left(\frac{\Gamma_{max}}{\Omega_e}\frac{n_0}{n_a}\right) \text{ at } L_c/2$$

t:				t_2									t_4					
r_m:	2			5			10			2			5			10		
N_c:	0	10	20	0	10	20	0	10	20	0	10	20	0	10	20	0	10	20
$U_{top} = 0.1$																		
U:	0.08			0.05			0.03			0.08			0.05			0.03		
$X1$:	-6.35	-6.46	-7.61	-5.44	-5.74	-6.74	-5.52	-5.46	-6.80	-3.89	-7.24	-7.94	-3.29	-6.14	-7.71	-3.52	-6.44	-8.01
$X2$:	-3.62	-5.17	-7.08	-3.18	-5.10	-7.16	-3.72	-5.54	-7.61	-2.89	-6.31	-7.99	-3.21	-6.84	-8.63	-3.86	-7.42	-9.17
$O1$:	-4.82	-5.23	-6.83	-4.03	-5.05	-6.69	-4.53	-5.50	-7.02	-2.81	-6.30	-7.77	-3.32	-6.25	-7.85	-4.05	-6.67	-8.15
$O2$:	-6.22	-6.36	-7.98	-5.41	-6.53	-8.10	-6.25	-6.98	-8.70	-4.61	-7.50	-8.89	-5.23	-7.93	-9.39	-5.88	-8.59	-9.92
$Z1$:	**-2.53**	**-4.10**	**-6.12**	**-1.88**	**-3.71**	**-5.75**	**-2.25**	**-4.14**	**-5.98**	**-1.53**	**-5.25**	**-6.93**	**-1.91**	**-5.17**	**-6.92**	**-2.33**	**-5.55**	**-7.21**
$U_{top} = 0.5$																		
U:	0.40			0.25			0.15			0.40			0.25			0.15		
$X1$:	*	*	-7.54	-4.67	-4.70	-5.54	-4.42	-4.44	-5.57	-9.49	-7.31	-8.54	-2.96	-5.06	-6.75	-3.00	-5.26	-6.86
$X2$:	-2.46	-4.34	-5.54	-1.94	-4.36	-5.53	-2.03	-4.60	-6.12	**-1.37**	-4.99	-6.68	-1.91	-5.47	-7.11	-2.25	-6.08	-7.89
$O1$:	-3.51	-4.10	**-5.30**	-2.58	-3.69	-5.32	-3.14	-4.02	-5.62	-1.50	-4.97	**-6.35**	-2.00	-4.85	-6.76	-2.66	-5.27	-6.84
$O2$:	-4.85	-5.01	-6.42	-4.00	-5.15	-6.72	-4.86	-5.56	-7.31	-3.25	-6.02	-7.51	-3.85	-6.56	-7.93	-4.49	-7.20	-8.52
$Z1$:	**-2.36**	**-4.07**	-5.56	**-1.63**	**-3.62**	**-5.08**	**-1.73**	**-3.79**	**-5.18**	-1.48	**-4.84**	**-6.35**	**-1.67**	**-4.61**	**-6.23**	**-1.82**	**-4.84**	**-6.39**
$U_{top} = 1.0$																		
U:	0.8			0.5			0.3			0.8			0.5			0.3		
$X1$:	*	*	*	**-9.16**	**-9.09**	**-8.63**	-4.97	-4.86	-5.21	*	*	*	-8.92	-8.87	-8.70	-4.80	-5.19	**-6.53**
$X2$:	**-1.33**	-3.55	**-5.31**	**-1.62**	**-3.37**	-5.17	-1.87	-3.85	-5.59	**-0.56**	-4.40	**-5.81**	**-1.24**	-5.06	-6.45	-2.00	-5.41	-7.14
$O1$:	-2.12	-4.21	-5.45	-2.44	-3.53	**-4.53**	-2.58	**-3.30**	-5.11	-1.10	-4.43	-6.27	-1.29	**-4.32**	**-5.61**	-2.09	**-4.79**	**-6.53**
$O2$:	-4.37	-4.76	-6.00	-3.39	-4.61	-6.21	-4.27	-4.91	-6.73	-2.78	-5.82	-6.88	-3.21	-5.96	-7.57	-3.92	-6.63	-7.93
$Z1$:	-1.99	**-3.39**	-6.13	-1.86	-3.76	-5.00	**-1.78**	-3.82	**-4.89**	-1.85	**-3.60**	-6.34	-1.77	-4.84	-6.16	**-1.80**	-5.24	-5.89

Values of the growth rate smaller than 10^{-10} are represented by an asterick.

Table 3

$$\log\left(\frac{\Gamma_{max}}{\omega_p}\right)$$

	r_m:	1			2			5			10		
	N_c:	0	10	20	0	10	20	0	10	20	0	10	20
$t = t_1$													
n_a/n_0	T												
10^{-2}	10^6	-3.22	-3.61	-4.41	-2.03	-2.76	-3.78	-2.81	-3.32	-3.88	-3.57	-3.94	-4.39
10^{-2}	10^7	-5.26	-5.26	-5.29	-2.22	-3.08	-4.01	-3.54	-3.70	-4.06	-5.24	-5.28	-5.34
10^{-4}	10^6	-5.35	-5.92	-6.41	-4.03	-4.76	-5.78	-4.81	-5.32	-5.88	-5.69	-5.94	-6.40
10^{-4}	10^7	-7.26	-7.26	-7.29	-5.07	-5.55	-6.22	-6.15	-6.27	-6.46	-7.27	-7.32	-7.38
$t = t_2$													
n_a/n_0	T												
10^{-2}	10^6	-2.32	-2.88	-3.42	-2.17	-4.48	*	-2.54	-3.82	-5.75	-2.85	-3.92	-5.66
10^{-2}	10^7	-2.84	-3.22	-3.66	*	*	*	*	*	*	*	*	*
10^{-4}	10^6	-4.32	-4.88	-5.42	-4.17	-7.57	*	-4.54	-5.82	-7.96	-4.85	-5.92	-7.66
10^{-4}	10^7	-5.18	-5.45	-5.98	*	*	*	*	*	*	*	*	*

Values of the growth rate smaller than 10^{-10} are represented by an asterick.

References

Aschwanden, M.J. 1989, (Preprint).

Aschwanden, M.J. and Benz, A.O. 1988, *Ap. J.*, **332**, 447.

Bastian, T.S. and Bookbinder, J.A. 1987, *Nature*, **326**, 678.

Benson, R.F., Calvert, W., and Klumpar, D.M. 1980, *Geophys. Res. Lett.*, **7**, 959.

Benz, A.O. 1986, *Solar Phys.*, **104**, 99.

Benz, A.O. and Kane, S.R. 1986, *Solar Phys.*, **104**, 179.

Brown, R.C. and Crane, P.C. 1978, *A.J.*, **83**, 1504.

Calvert, W. 1981, *J. Geophys. Res.*, **86**, 76.

Carr, T.D., Desch, M.D., and Alexander, J.K. 1983, in Dessler, A.J. (ed.), *Physics of the Jovian Magnetosphere*, (New York: Cambridge University Press), p. 226.

Dröge, F. 1977, *Astr. Ap.*, **57**, 285.

Freund, H.P., Wong, H.K., Wu, C.S., and Xu, M.J. 1983, *Phys. Fluids*, **26**, 2263.

Goldman, M.V. and Smith, D.F. 1986, in P.A. Sturrock (ed.), *Physics of the Sun*, (Boston: D.Reidel Publishing Company), Vol. II, p. 325.

Gurnett, D.A. 1974, *J. Geophys. Res.*, **79**, 4227.

Gurnett, D.A., Kurth, W.S., Scarf, F.L., and Poynter, R.L. 1986, *Science*, **233**, 106.

Hamilton, R.J. and Petrosian, V. 1987, *Ap. J.*, **321**, 721.

Hamilton, R.J., Lu, E.T., and Petrosian, V. 1990, *Ap. J.*, in press.

Hewitt, R.G., Melrose, D.B., and Rönnmark, K.G. 1982, *Aust. J. Phys.*, **35**, 447.

Holman, G.D., Eichler, D., and Kundu, M.R. 1980, in M. Kundu and T. Gergely (ed.), *IAU Symposium 86, Radio Physics of the Sun*, (Dordrecht: Reidel Publishing Company), p. 457.

Kaiser, M.L., Desch, M.D., Kurth, W.S., Lecacheux, A., Genova, F., Pedersen, B.M., and Evans, D.R. 1984, in Gehrels, T. and Matthews, M.S. (eds.), *Saturn*, (Tucson: The University of Arizona Press), p. 378.

Kane, S.R. *et al.*1980, in P.A. Sturrock (ed.), *Solar Flares*, (Boulder: Colorado Assoc. Univ. Press), p. 187.

Kuijpers, J., van der Post, P., and Slottje, C. 1981, *Astr. Ap.*, **103**, 331.

Kundu, M.R. and Shevgaonkar, R.K. 1988, *Ap. J.*, **334**, 1001.

Lang, R.L. and Wilson, R.F. 1986, *Ap. J.*, **305**, 363.

Leach, J. and Petrosian, V. 1981, *Ap. J.*, **251**, 781.

Lee, L.C. and Wu, C.S. 1980, *Phys. Fluids*, **23**, 1348.

Lestrade, J., Mutel, R.L., Preston, R.A., and Phillips, R.B. 1988, *Ap. J.*, **328**, 232.

McClements, K.G. 1987, *Solar Phys.*, **109**, 355.

Melrose, D.B. 1980, *Plasma Astrophysics I*, (New York: Gordon and Breach Science Publishers).

Melrose, D.B. and Dulk, G.A. 1982a, *Ap. J.*, **259**, 844.

Melrose, D.B. and Dulk, G.A. 1982b, *Ap. J. (Letters)*, **259**, L41.

Melrose, D.B., Hewitt, R.G., and Dulk, G.A. 1984, *J. Geophys. Res.*, **89**, 897.

McTiernan, J.M. and Petrosian, V. 1989, Submitted for publication.

Omidi, N. and Gurnett, D.A. 1984, *J. Geophys. Res.*, **89**, 10801.

Schrijver, C.J., Lemen, J.R., and Mewe, R. 1989, *Ap. J.*, **341**, 484.

Sharma, R.R., Vlahos, L., and Papadopoulos, K. 1982, *Astr. Ap.*, **112**, 377.

Slottje, C. 1978, *Nature*, **275**, 520.

Sprangle, P. and Vlahos, L. 1983, *Ap. J. (Letters)*, **273**, L95.

Stähli, M. and Magun, A. 1986, *Solar Phys.*, **104**, 117.

Stix, T.H. 1962, *The Theory of Plasma Waves*, (San Francisco: McGraw-Hill Book Company, Inc.).

White, S.M., Melrose, D.B., and Dulk, G.A. 1983, *Proc. Astr. Soc. Australia*, **5**, 188.

White, S.M., Melrose, D.B., and Dulk, G.A. 1986, *Ap. J.*, **308**, 424.

Wu, C.S. and Lee, L.C. 1979, *Ap. J.*, **230**, 621.

Wu, C.S., Wong, H.K., Gorney, D.J., and Lee, L.C. 1982, *J. Geophys. Res.*, **87**, 4476.

Wu, C.S. 1985, *Space Sci. Rev.*, **41**, 215.

Zhao, R. 1983, *Adv. Space Res.*, Vol. 2, **11**, p. 177.

Zhao, R. and Jin, S. 1982, *Scientia Sinica*, **15**, 422.

Figure Captions

Fig. 1. Contour plots of the electron distribution function in the $\beta_{\|}$–$\beta_{\perp}$ plane at the top of the loop for a mirror ratio of $r_m = 5$. The column depths from left to right are $N_{tr} =$ 0, 1.88×10^{19}, and $7.37 \times 10^{19}\mathrm{cm}^{-2}$ corresponding to stopping depths for electrons of energies $E = 0$, 10, and 20 keV, respectively. The times from top to bottom are $\frac{1}{6}T_B^{max}$, $\frac{1}{2}T_B^{max}$, T_B^{max}, and $\frac{3}{2}T_B^{max}$. The contour levels are spaced by a factor of 10 and are the same for each plot.

Fig. 2. Same as Figure 1, but at $s = L_c/2$.

Fig. 3. Contour plot of the electron distribution shown in the middle of Figure 2 with $N_{tr} = 1.88 \times 10^{19}\mathrm{cm}^{-2}$ at time $\frac{3}{2}T_B^{max}$. Contour levels are now spaced by a factor of 5. The darker lines represent the resonant ellipses of the o-mode (s=1), x-mode (s=2), and z-mode waves at frequencies and angles which maximize their growth rates.

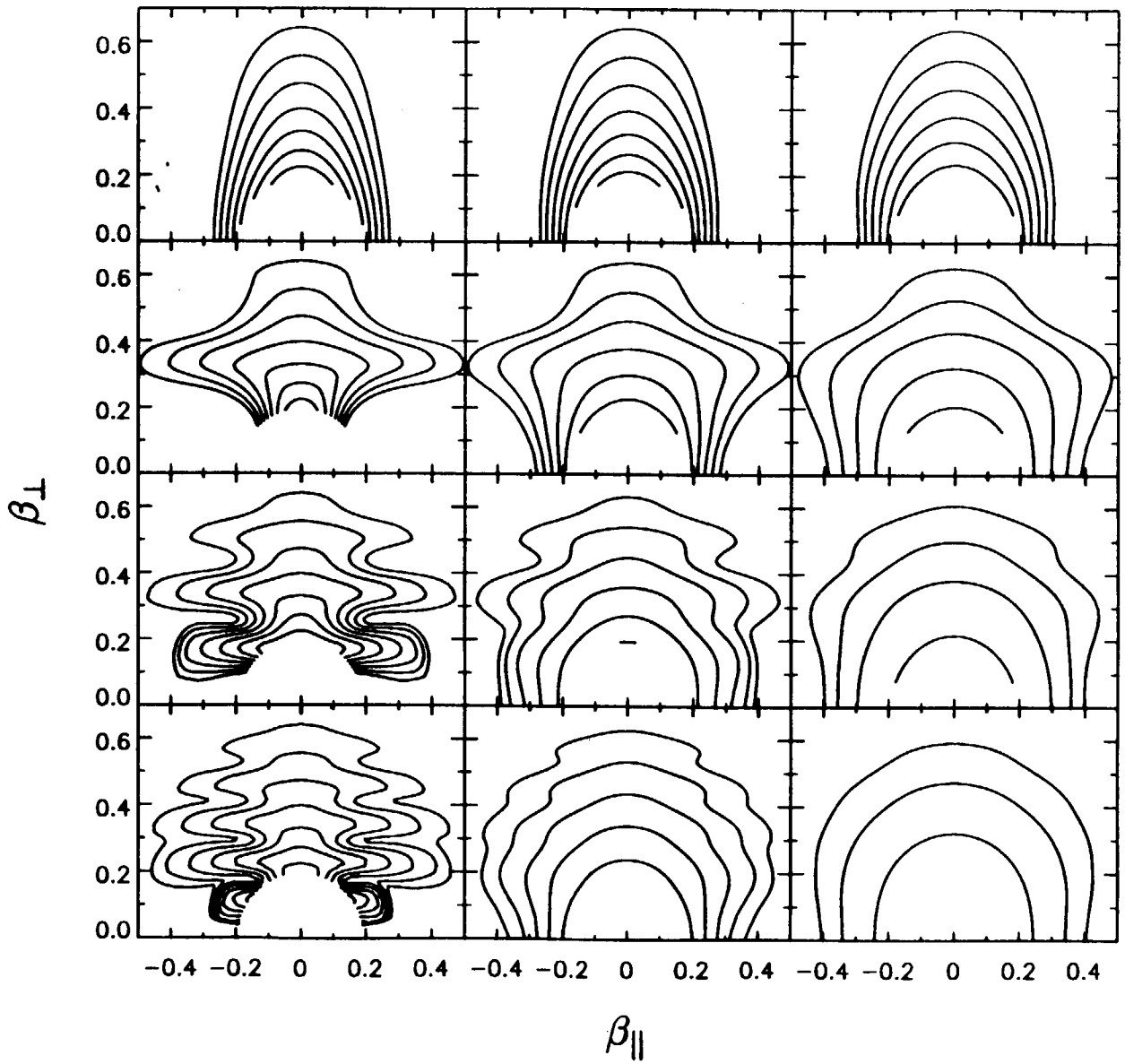
0.6
0.4
0.2
0.0
−0.4 −0.2 0 0.2 0.4
$\beta_\perp$
$\beta_{||}$

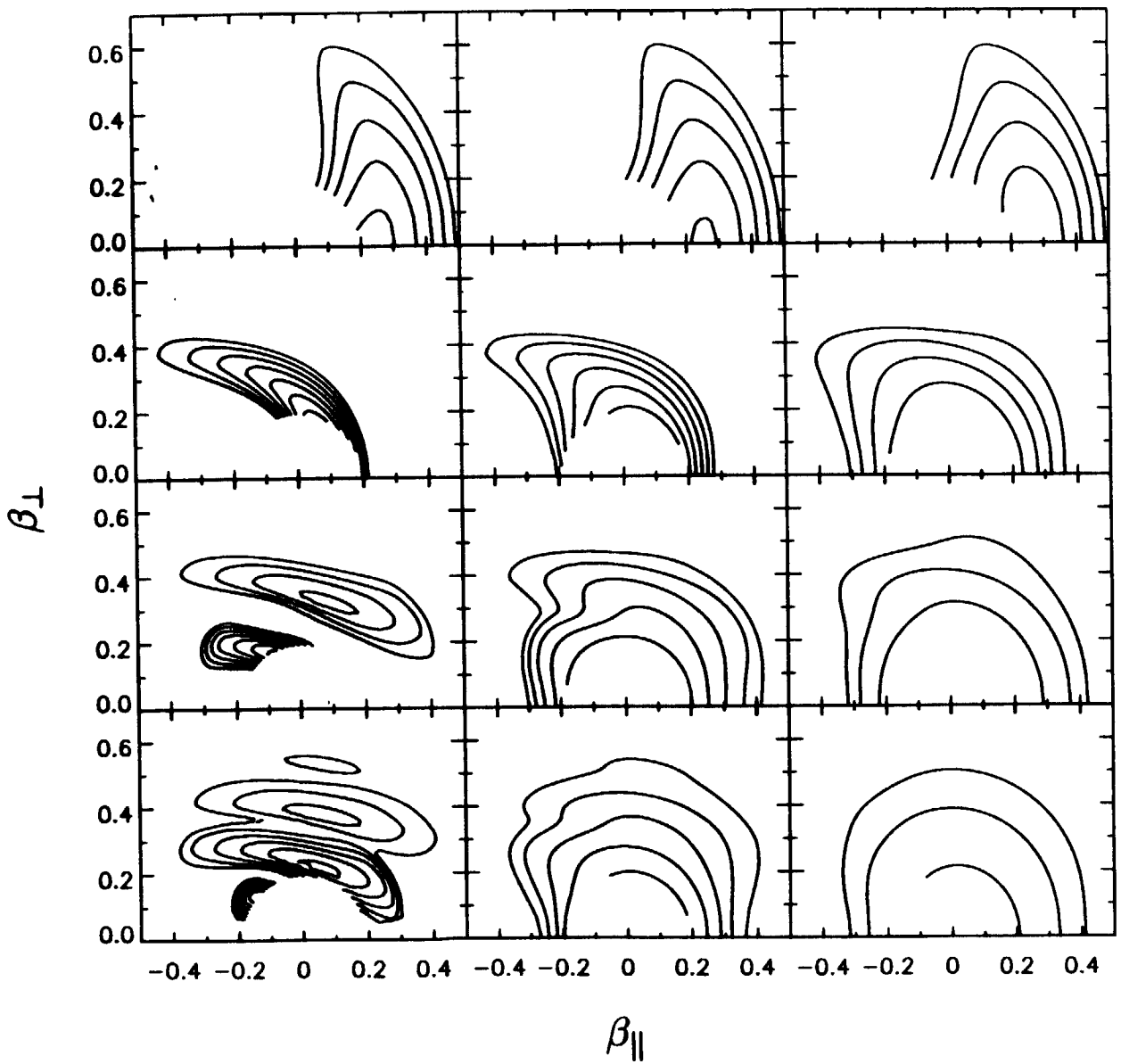
0.6
0.4
0.2
0.0
$\beta_\perp$
−0.4 −0.2 0 0.2 0.4
$\beta_{||}$

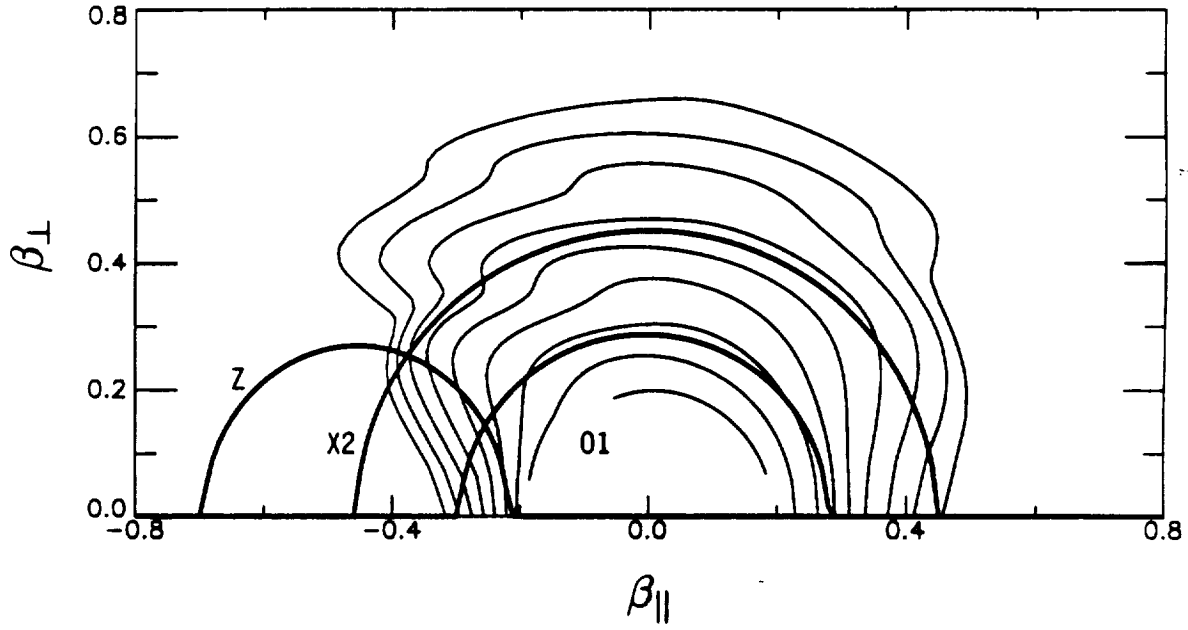
0.8
0.6
0.4
0.2
0.0
$\beta_\perp$
Z
X2
O1
−0.8
−0.4
0.0
0.4
0.8
$\beta_{||}$